nature methods

Article

https://doi.org/10.1038/s41592-025-02849-2

Spatiotemporal focusing enables all-optical in situ histology of heterogeneous tissue

Received: 8 November 2024

Xiang Ji **©** ¹⊠, Sincheng Huang **©** ¹, Beth Friedman ² & David Kleinfeld **©** ^{1,3}⊠

Accepted: 20 August 2025

Published online: 3 October 2025



Living systems embody heterogeneous tissues with complex opto-mechanical properties. Achieving organ-scale, diffraction-limited volumetric imaging that faithfully captures in vivo architecture requires minimizing sample deformation and preserving vascular and neuronal continuity across delicate tissue interfaces. As a solution to this problem, we developed a robotic nonlinear optical system for iterative multiphoton microscopy and opto-micromachining. Adaptive control enabled days-long autonomous operation, while spatiotemporal line-focused ablation increased the machining efficiency by 100-fold over prior configurations. Using the intact murine craniocerebral system as a test bed, our approach demonstrates the potential for whole-body submicrometer resolution imaging and anatomical reconstruction.

Complex living systems, such as vertebrates, consist of heterogeneous tissues whose detailed composition and spatial organization give rise to diverse biological functions. Precision measurement of three-dimensional (3D) structures has been instrumental in advancing biomedical science, from tracing neural circuitry to diagnosing disease. The past decade has witnessed the rapid development of optical microscopy and tissue clearing techniques that collectively enabled large-scale 3D histology. By homogenizing the refractive index in the preparation¹, tissue clearing substantially reduces wavefront distortion and increases light penetration to enable millimeter-scale tissue imaging at cellular resolution²⁻⁴. Yet for submicrometer resolution imaging on the scale of whole organs, as required for high-quality morphological reconstruction of brain-wide neuronal projections⁵⁻⁷ and vascular connectomes⁸⁻¹⁰, iterative imaging and tissue-sectioning techniques¹¹ are commonly applied.

Because tissue heterogeneity might pose a practical limit on tissue clearing, recent advances in large-scale tissue imaging involved the development of vibratomes for sectioning tissue, for example, the human hemisphere, with greater size, speed and flatness^{12,13}. However, vibration-based sectioning is not suitable for hard materials, such as bone, because high sample resistance disrupts accuracy^{12–14}. To fill the gap of submicrometer resolution 3D imaging of large-scale heterogeneous samples, such as the craniocerebral system, we developed a smart robotic nonlinear optical platform.

Results

We integrated diffraction-limited scanning multiphoton microscopy¹⁵ with a temporal-focusing-based^{16–18} laser micromachining system (Fig. 1a). Imaging involved backscattered second harmonic generation (SHG) by bone and intrinsic or labeled fluorescence of soft tissue. Micromachining made use of tightly focused ultrafast laser pulses to produce highly localized plasma through nonlinear absorption processes. This allowed us to remove target material with diffraction-limited precision^{19,20}. To scale up ablation efficiency while preserving the necessary axial machining precision for serial volumetric imaging, we applied simultaneous spatiotemporal focusing for pulse shaping. A diffraction grating stretched the pulse width by over an order of magnitude, and a '4f' system consisting of a cylindrical lens and a high numerical aperture (NA) objective reconstructed the line-shaped femtosecond pulse on the imaging focal plane.

Submicrometer resolution imaging requires the use of a high NA objective in immersion medium, yet femtosecond laser ablation in an aqueous environment produces cavitation bubbles. These bubbles accumulate on both the objective and sample surface, potentially interrupting continuous machining within seconds and interfering with the subsequent imaging (Extended Data Fig. 1). To ameliorate this problem, we incorporated a compact closed-loop flow system to flush laser-induced cavitation bubbles and sample debris. This involved screening index-matching solutions for low viscosity,

¹Department of Physics, University of California San Diego, La Jolla, CA, USA. ²Department of Computer Science and Engineering, University of California San Diego, La Jolla, CA, USA. ³Department of Neurobiology, University of California San Diego, La Jolla, CA, USA. ⊠e-mail: xij072@ucsd.edu; dk@physics.ucsd.edu

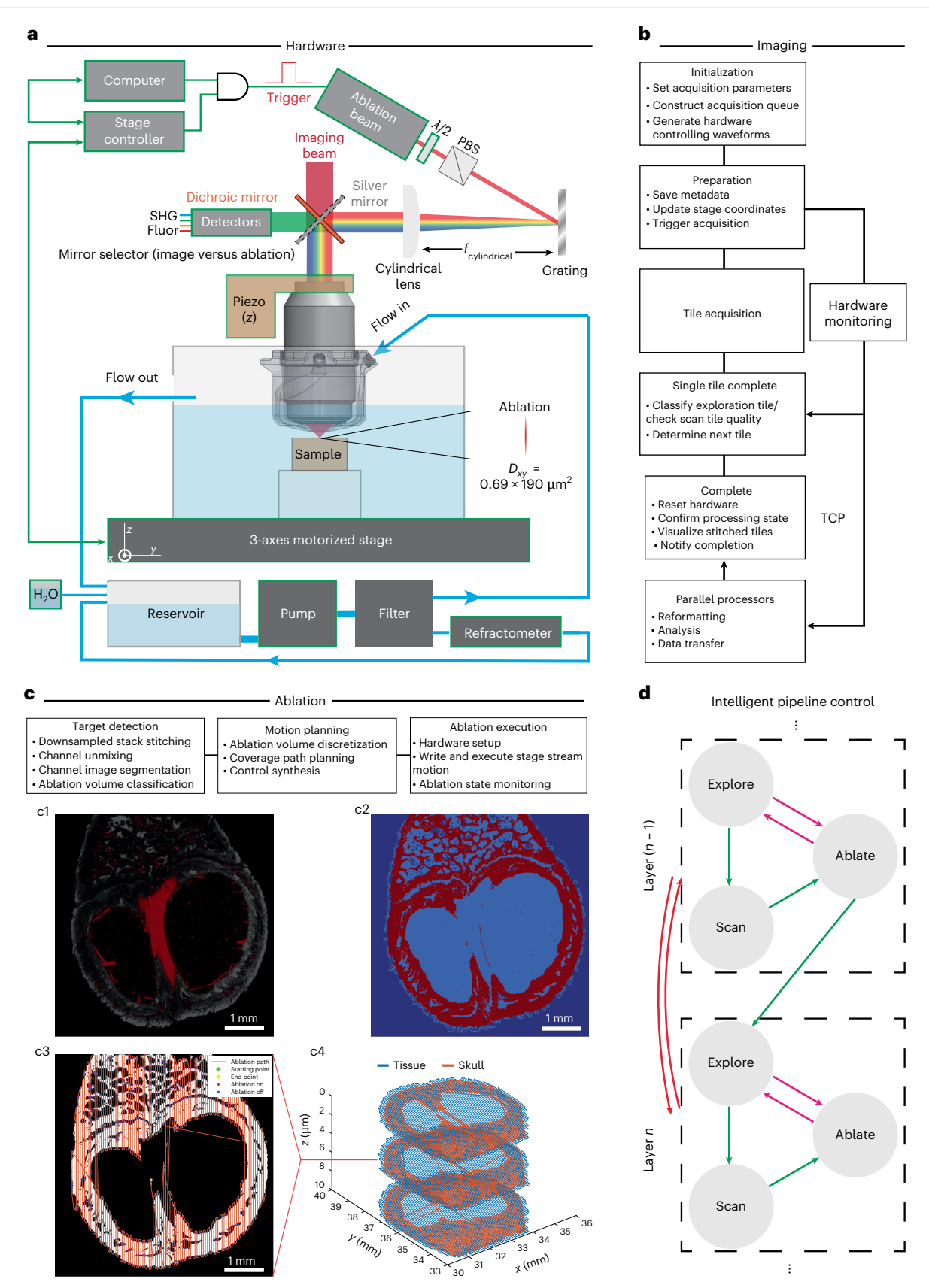


Fig. 1| **System hardware schematic and smart control software illustration. a**, System hardware. The grating surface is conjugated to the imaging plane to form a line pattern. An actuator toggles between imaging dichroic and ablation mirror. The computer controls the green-boxed components. Beam size in the lateral plane, denoted D_{xy} , corresponds to the dimensions at $1/e^2$ of the maximum intensity, $\lambda/2$ is a half-wave plate, PBS is a polarizing beam splitter and piezo(z) is an axial actuator. **b**, Imaging control workflow. TCP, transmission control

protocol. \mathbf{c} , Ablation control workflow (c1: single image of the mouse brain vasculature (red) in the skull (gray) in the horizontal plane; c2: classification of pixels to assign material-specific machining parameters; c3: coverage machining path planning; and c4: machining trajectories covering different materials). \mathbf{d} , System state workflow. Acquisition is divided into multiple layers. Normal workflow (green arrows) involves iterative exploration, scanning and ablation. The exploration results are also used for machining quality control (red arrows).

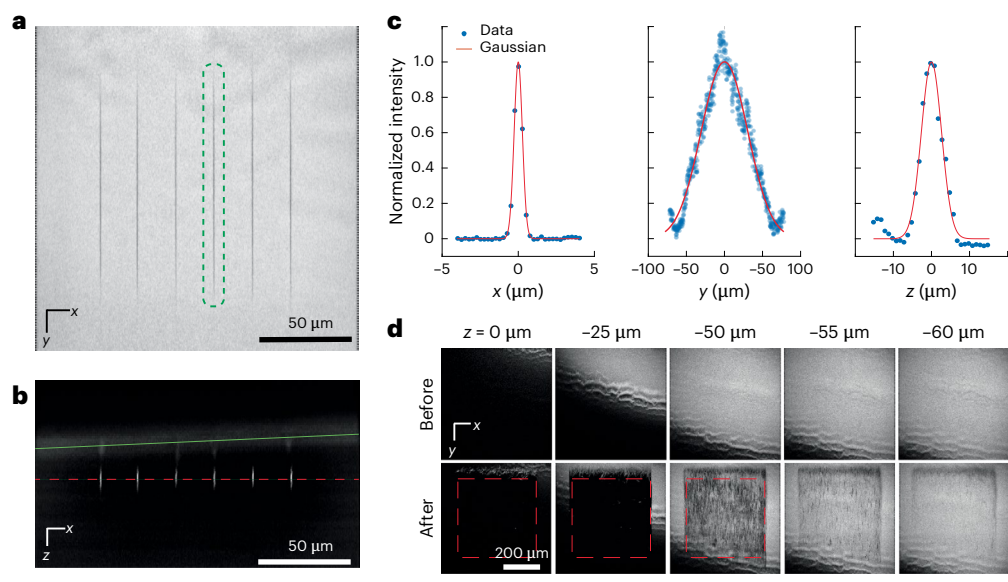


Fig. 2| **Experimental test results. a**, A gelatin block after six single-pulse ablations. **b**, Side (x, z) view of the intensity difference before and after ablation in **a**. The ablation plane (red dashed line) is 15 μ m below the gelatin surface (green line). **c**, Profile of the intensity difference before and after ablation of

one ablation site (highlighted by the green dashed outline in **a**). Gaussian fit FWHM $_{xyz}$ = [0.63, 72.1, 6.23] μ m. **d**, A gelatin block before and after continuous ablation (500 × 500 × 50 μ m³). The red dashed boxes indicate the ablation region.

low vapor pressure and high ablation threshold (Fig. 1a). We selected dimethyl sulfoxide (DMSO) in aqueous buffer, with n = 1.4286. An artificial vision-based feedback control system further maintained the refractive index of the solution over an extended period (coefficient of variation of 0.00016 over 96 h; Extended Data Fig. 2h).

We developed a suite of open-source software to enable robust multi-day autonomous operation and efficient data handling. The acquisition volume was divided into multiple partially overlapping layers (Fig. 1b). In each layer, the microscope explored the sample surface, scanned the volumes of interest at high resolution, analyzed the images using an online processing pipeline and ablated the targeted volume (Fig. 1c,d). To ensure flawless imaging over days, the software periodically probed hardware states (Extended Data Fig. 2) and analyzed images to detect and autonomously handle hardware abnormalities. The resulting multichannel images were segmented, and voxels were classified and assigned material-specific machining parameters (Fig. 1c). The software then discretized the targeted volume, optimized the machining trajectory, synthesized low-level hardware control sequences (Fig. 1c) and executed the sequences while monitoring system status. To ensure clean machining and optimal imaging quality, exploration images were used to determine if additional refinements with adjusted machining parameters were needed (Extended Data Fig. 2a-f).

We first evaluated the feasibility of the ablation system (Fig. 1) and characterized its precision. Using a fluorescent gelatin block, we assessed single-pulse-induced ablation on a plane ~15 μm below the surface (Fig. 2a,b). Each pulse reliably produced a line-ablation pattern with no visible damage to the adjacent volume. All the ablation sites were located precisely on the designated ablation plane despite having varying thicknesses of gelatin above. We estimated the full-width-at-half-maximum (FWHM) diameter of the ablation volume to be $\Delta x = 0.62 \pm 0.01 \,\mu m$ (mean \pm s.e.m.), $\Delta y = 71 \pm 4 \,\mu m$ and $\Delta z = 6.1 \pm 0.5 \,\mu m$ (Fig. 2c). These dimensions were consistent with the designed pattern. Our data show that single femtosecond pulses can reliably produce line-ablation patterns in a scattering gelatin block with high spatial precision. This configuration increased single-pulse ablation efficiency by over 100-fold compared to a Gaussian-focused volume of a similar axial confinement 21 .

We then used a gelatin block and a rodent skull to test continuous volumetric ablation in samples of distinct opto-mechanical properties.

Starting from the plane above the sample surface, we ablated gelatin and skull at rates of $7.7 \times 10^5 \, \mu m^3 \, s^{-1}$ and $1.4 \times 10^5 \, \mu m^3 \, s^{-1}$, respectively. The ablation process removed the targeted volume with no visible lateral damage, while axial damage was confined to within 5 μ m below the last ablation plane (Fig. 2d). Microcavities in the skull at a depth of ~50 μ m were clearly resolved after removing the upper 45 μ m of the skull (Extended Data Fig. 3). We further explored planar ablation using a spherical lens in the 4f system (Extended Data Fig. 4). This configuration produced an intermediate line focus that risked damaging the objective, which we mitigated by using a small-angle diffuser. This approach increased ablation efficiency by another 100-fold and produced a sharp lateral boundary of the ablation volume. However, it did not adequately confine out-of-focus damages (Extended Data Fig. 5). Overall, line ablation offers the best trade-off between efficiency and spatial precision (Extended Data Fig. 4).

Finally, we imaged and ablated the craniocerebral vascular network from the outer surface of the skull down to the white matter (Extended Data Fig. 6); the experimental parameters are listed in Supplementary Tables 1 and 2. Skull and fluorescein-labeled vasculature were imaged at $0.35 \times 0.35 \times 1.0 \,\mu\text{m}^3$ resolution. Using features from the skull and vessels in the overlapping volume of adjacent image tiles, we computed the nonrigid deformation field and smoothly stitched all image tiles into a single coherent volume of 5.4 × 4.2 × 1.8 mm³ (Supplementary Video 1). A representative image of a single horizontal section demonstrates a uniform imaging quality throughout the entire cross-section (Fig. 3a-c). Simultaneous two-color imaging shows the intricate vascular connections on the brain-skull interface and detailed layering and bone fiber orientation in the skull (Fig. 3c,d). Reprojections on the coronal plane (Fig. 3e) further highlighted vessels in the craniocerebral system (Fig. 3f-i), notably a meningeal vessel and a pial vessel separated by the meningeal collagen layer (Fig. 3g). Collectively, these results demonstrate that the current system enables imaging of an extended volume of heterogeneous biological tissue with a uniform submicrometer resolution.

Discussion

We developed a femtosecond laser ablation system optimized for large-scale precision micromachining of heterogeneous materials in an aqueous environment. Despite a 100-fold improvement in ablation efficiency over prior schemes that used a Gaussian beam,

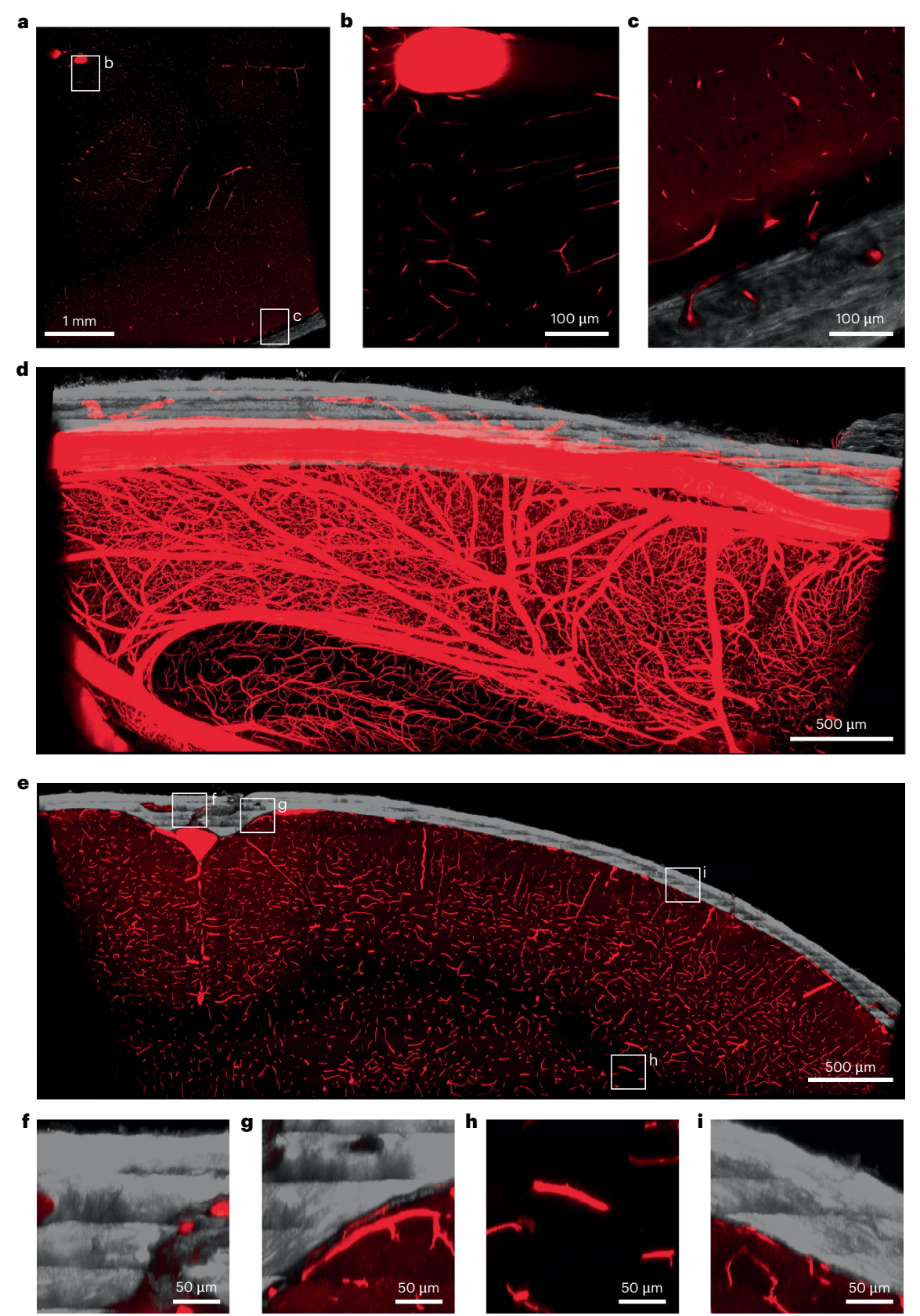


Fig. 3 | **In situ imaging results. a**, Imaging of mouse brain vasculature (red) and skull (gray) at $0.35 \times 0.35 \times 1.0 \ \mu\text{m}^3$ resolution on the horizontal plane. Similarly sized volumes (**b**-**d**) were obtained from five mice. **b**, Image showing the vasculature near the sinuses at 1.8 mm below the skull surface (white-boxed in **a**). **c**. Image showing fine bone fiber structures and microvessels in skull cavities (white-boxed in **a**). **d**, Maximum-intensity projection (150 μ m) of the craniocerebral system on the sagittal plane. Image volume resampled at 1.0 × 1.0

 $\times\,1.0~\mu\text{m}^3$ voxel resolution (same for e). e, Maximum-intensity projection (20 $\mu\text{m})$ of the craniocerebral system (a) in the coronal plane. f, Image showing the vessels inside the skull above the sagittal sinus (white-boxed in e). g, Image showing a meningeal vessel and a pial vessel separated by the meningeal collagen layer with weak SHG signal (white-boxed in e). h, Image showing microvessels in the white matter (white-boxed in e). i, Image showing the brain–skull interface (white-boxed in e).

Table 1 | Comparison of methods for volumetric tissue removal

	Line-focused ablation (this work)	Vibratome	Microtome	Tissue mill	Photodegradation	Focused ion beam
Sectioning speed (μm³ s ⁻¹)	1.0×10 ⁶ (soft tissue) 1.4×10 ⁵ (skull) Potentially up to ^a 1×10 ⁸ (soft tissue) 1×10 ⁷ (skull)	Effective rate ^b : 1×10 ⁸ to 2×10 ⁹	Effective rate ^c : 1.3×10 ⁶ to 4.5×10 ⁶	Effective rate ^d : 4.3×10 ⁸	Light-sheet illumination pre-expansion rate°: 5.0×10 ⁵ Two-photon illumination pre-expansion rate°: 8×10 ²	30-nA milling probe ²⁵ : 50
Sectioning volume control	Arbitrary volumes	Planar cutting	Planar cutting	Planar cutting	Planar cutting or arbitrary volumes	Planar cutting
Sample preparation	Perfusion and optional post-fixation of tissue	Tissue fixation Agarose/hydrogel embedding Tissue clearing ²⁶ EDTA for decalcification ²⁶	Tissue fixation Resin embedding Dehydration	Tissue fixation Organogel ²⁷ / paraffin ²⁸ embedding Tissue clearing Dehydration	Tissue fixation Phosphorylcholine hydrogel expansion	Tissue fixation Heavy metal staining Epoxy embedding Dehydration
Total sample deformation	Apparently minimal because optical ablation is noncontact and minimal sample preparation is required	Deformations caused by mechanically cutting heterogeneous tissue ²⁹ Deformations related to sample preparation	Deformations caused by mechanically cutting heterogeneous tissue Deformations related to sample preparation, such as uneven shrinkage ²⁷	Deformations caused by milling unknown Deformations related to sample preparation, such as uneven shrinkage ²⁷	Deformations caused by photodegradation unknown ^f Deformations related to hydrogel expansion ³⁰	Deformations such as streaks ²⁵ and from sample embedding ³¹
		No apparent limitations	Fluorescence quenched but can be chemically reactivated ³²	No apparent limitations	Avoid photodegradation wavelengths	N/A
Tissue heterogeneity	Potentially anything by optimizing parameters	Soft tissue, bone (if decalcified) ²⁶	Any tissue as long as uniformly rigidified ²⁷	Any tissue as long as uniformly rigidified ²⁷	Soft tissue Skull unknown ⁹²⁷	Soft tissue, bone 33
Tissue interface preservation	Apparently preserved	Potential enlargement of the interface between different tissue types ^h	Uneven tissue shrinkage among different tissue types potentially affects tissue interfaces ²⁷	Uneven tissue shrinkage among different tissue types potentially affects tissue interfaces ²⁷	Unknown ⁱ	Unknown

The 1-kHz femtosecond laser (Astrella, Coherent) can be replaced by a 1-MHz femtosecond laser (Monaco, Coherent) for a potential increase of up to ×100 (Supplementary Table 2); however, this has vet to be demonstrated. Li et al. High implemented a 180-Hz flexure-based vibratome and estimated rates of 20 × 11 × 8 mm³ in 3.3 h. or approximately 1 × 108 um³ s 1, for a mouse brain. For a human brain, they estimated a rate of 167×149×93mm³ in 436h, corresponding to 1.5×109 µm³s¹. A recent work by Shi et al.26 used a vibratome alongside clearing and decalcification for high-speed imaging of an entire mouse. They sectioned a $4 \text{cm} \times 2 \text{cm} \times 400 - \mu \text{m}$ volume in 3 min, resulting in a rate of about $2 \times 10^9 \, \mu \text{m}^3 \, \text{s}^{-1}$. Moreover, the MEGAtome platform implemented by Park et al. 12 can simultaneously section 35 mouse brains in an array. In general, vibratomes easily scale to sectioning larger volumes, although sectioning thickness is fundamentally tied to imaging depth and resolution. 'The MOST system' sectioned and imaged a resin-embedded mouse brain sample with 11.3×6.6×14.8-mm³ volume over 242h, yielding an effective rate of 1.3×106 µm3s-1. As imaging and sectioning occur simultaneously, it is difficult to estimate the time required for sectioning alone. In the HD-fMOST system14, sectioning and imaging are separate. Each 2-µm thick coronal layer contained 8.5 strips that measured 660 µm×10 mm and were sectioned in 25 s, resulting in a sectioning rate of 4.5×106 µm² s⁻¹. dRagan et al. 28 used a 3/8-in diameter milling bit, removing 45 µm per layer, with a feed rate of 1mms⁻¹, resulting in a rate of tissue removal of 4.3×108 µm³s⁻¹. Wang et al. 40 monstrated the use of photochemical degradation in hydrogel-expanded samples as a means of tissue sectioning. A light-sheet photodegradation illumination scheme sectioned a 3,320×4,870×2,220 µm³ sample of mouse olfactory bulb in 20h, yielding a rate of 5.0×105 µm3 s-1. On the other hand, a two-photon photodegradation illumination scheme sectioned a 5.4-times expanded sample of a mouse brain slice, measuring 600×1,260×3,800 µm³, in 6h; this corresponds to a rate of 8×10² µm³s⁻¹. Wang et al. 50 noted the presence of nonrigid deformations. Deformations from sectioning are likely to be minimal because photodegradation is noncontact. 9Whole-body expansion has recently been demonstrated in embryos and neonates 30. Therefore, it is possible that samples with bone can also be photodegraded, but this has yet to be demonstrated. To our knowledge, the only attempt to section a sample with both soft tissue and bone is demonstrated in the work by Shi et al.26. The gap between the brain parenchymal surface and the skull is larger than expected, suggesting that relative tissue distortions between the two interfaces may have occurred, potentially caused by uneven tissue expansion or shrinkage of different tissue types during and after delipidation, washing and refractive index matching26. Thus, anatomical structures between the brain and skull may be broken or distorted. 'Sim et al.30 selected 11 regions proximal to bone and soft tissue interfaces and quantified a root mean squared error of 6.7% comparing before and after expansion.

there are several potential means to further enhance ablation efficiency. A higher-repetition-rate femtosecond laser can likely increase ablation efficiency (Supplementary Table 3). However, the interactions between cavitation bubbles could limit the maximum repetition rate²².

To our knowledge, all-optical serial two-photon microscopy is the only optical approach to achieve submicrometer resolution in situ imaging of the craniocerebral system. While pioneering femtosecond laser micromachining efforts were applied to homogeneous samples 19,20,23,24, the current approach enabled micromachining to

be applied to both large-scale and inhomogeneous tissues. Selected subvolumes within an otherwise intact organ can be imaged. More so, all-optical serial two-photon microscopy involves minimal sample preparation that preserves the anatomical integrity of all tissues and, critically, the interface of different tissues. These advances come at the cost of not retaining tissue for post-hoc analysis (a comparison of strengths and weaknesses across existing volumetric anatomical methods is given in Table 1). Nonetheless, our results support the potential of our approach for whole-body submicrometer resolution imaging and anatomical reconstruction.

Online content

Any methods, additional references, Nature Portfolio reporting summaries, source data, extended data, supplementary information, acknowledgements, peer review information; details of author contributions and competing interests; and statements of data and code availability are available at https://doi.org/10.1038/s41592-025-02849-2.

References

- Richardson, D. S. & Lichtman, J. W. Clarifying tissue clearing. Cell 162, 246–257 (2015).
- Tsai, P. S. et al. Correlations of neuronal and microvascular densities in murine cortex revealed by direct counting and colocalization of cell nuclei and microvessels. J. Neurosci. 18, 14553–14570 (2009).
- 3. Ueda, H. R. et al. Tissue clearing and its applications in neuroscience. *Nat. Rev. Neurosci.* **21**, 61–79 (2020).
- Renier, N. et al. iDISCO: a simple, rapid method to immunolabel large tissue samples for volume imaging. Cell 159, 896–910 (2014).
- Winnubst, J. et al. Reconstruction of 1,000 projection neurons reveals new cell types and organization of long-range connectivity in the mouse brain. Cell 179, 268–281 (2019).
- Peng, H. et al. Morphological diversity of single neurons in molecularly defined cell types. Nature 598, 174–181 (2021).
- Gao, L. et al. Single-neuron projectome of mouse prefrontal cortex. Nat. Neurosci. 25, 515–529 (2022).
- Ji, X. et al. The brain microvasculature has a common topology with local differences in geometry that match metabolic load. Neuron 109, 1168–1187 (2021).
- Ragan, T. et al. Serial two-photon tomography for automated ex vivo mouse brain imaging. Nat. Methods 9, 255–258 (2012).
- Economo, M. N. et al. A platform for brain-wide imaging and reconstruction of individual neurons. eLife 5, e10566 (2016).
- Li, A. et al. Micro-optical sectioning tomography to obtain a highresolution atlas of the mouse brain. Science 330, 1404–1408 (2010).
- Park, J. et al. Integrated platform for multiscale molecular imaging and phenotyping of the human brain. Science 384, eadh9979 (2024).
- Chang, S. et al. Multi-scale label-free human brain imaging with integrated serial sectioning polarization sensitive optical coherence tomography and two-photon microscopy. Adv. Sci. 10, e2303381 (2023).
- Zhong, Q. et al. High-definition imaging using line-illumination modulation microscopy. Nat. Methods 18, 309–315 (2021).
- Denk, W., Strickler, J. H. & Webb, W. W. Two-photon laser scanning fluorescence microscopy. Science 248, 73–76 (1990).
- Oron, D., Tal, E. & Silberberg, Y. Scanningless depth-resolved microscopy. Opt. Express 13, 1468–1476 (2005).
- Zhu, G., van Howe, J., Durst, M., Zipfel, W. & Xu, C. Simultaneous spatial and temporal focusing of femtosecond pulses. Opt. Express 13, 2153–2159 (2005).
- Durst, M. E., Zhu, G. & Xu, C. Simultaneous spatial and temporal focusing in nonlinear microscopy. Opt. Commun. 281, 1796–1805 (2008).
- Gattass, R. R. & Mazur, E. Femtosecond laser micromachining in transparent materials. Nat. Photonics 2, 219–225 (2008).

- Tsai, P. S. et al. Plasma-mediated ablation: an optical tool for submicrometer surgery on neuronal and vascular systems. Curr. Opin. Biotechnol. 20, 90–99 (2009).
- 21. Tsai, P. S. et al. All-optical histology using ultrashort laser pulses. *Neuron* **39**, 27–41 (2003).
- 22. Mortensen, L. J. et al. Femtosecond laser bone ablation with a high repetition rate fiber laser source. *Biomed. Opt. Express* **6**, 32–42 (2014).
- 23. Vogel, A., Noack, J., Huttman, G. & Paltauf, G. Mechanisms of femtosecond laser nanosurgery of cells and tissues. *Appl. Phys. B* **81**, 1015–1047 (2005).
- 24. Jeong, D. C., Tsai, P. S. & Kleinfeld, D. All-optical osteotomy to create windows for transcranial imaging in mice. *Opt. Express* 21, 23160–23168 (2013).
- Xu, C. S., Pang, S., Hayworth, K. J. & Hess, H. F. in Volume Microscopy Vol. 155 (eds Wacker, I. et al.) 221–243 (Springer, 2020).
- 26. Shi, M.-Y. High-speed mapping of whole-mouse peripheral nerves at subcellular resolution. *Cell* **188**, 3897–3915 (2025).
- Yi, Y. et al. Mapping of individual sensory nerve axons from digits to spinal cord with the transparent embedding solvent system. Cell Res. 34, 124–139 (2024).
- Ragan, T. et al. High-resolution whole organ imaging using two-photon tissue cytometry. J. Biomed. Opt. 12, e014015 (2007).
- Ma, C. et al. High precision vibration sectioning for 3D imaging of the whole central nervous system. J. Neurosci. Methods 399, e109966 (2023).
- Sim, J. et al. Nanoscale resolution imaging of whole mouse embryos using expansion microscopy. ACS Nano 19, 7910–7927 (2025).
- Tegethoff, L. & Briggman, K. L. Quantitative evaluation of embedding resins for volume electron microscopy. Front. Neurosci. 18, 1286991 (2024).
- 32. Xiong, H. et al. Chemical reactivation of quenched fluorescent protein molecules enables resin-embedded fluorescence microimaging. *Nat. Commun.* **5**, e3992 (2014).
- Schneider, P., Meier, M., Wepf, R. & Müller, R. Serial FIB/SEM imaging for quantitative 3D assessment of the osteocyte lacuno-canalicular network. *Bone* 49, 304–311 (2011).
- 34. Li, Y. et al. Precision vibratome for high-speed ultrathin biotissue cutting and organ-wide imaging. *iScience* **24**, e103016 (2021).
- 35. Wang, W. et al. Nanoscale volumetric fluorescence imaging via photochemical sectioning. Preprint at *bioRxiv* https://doi.org/10.1101/2024.08.01.605857 (2024).

Publisher's note Springer Nature remains neutral with regard to jurisdictional claims in published maps and institutional affiliations.

Springer Nature or its licensor (e.g. a society or other partner) holds exclusive rights to this article under a publishing agreement with the author(s) or other rightsholder(s); author self-archiving of the accepted manuscript version of this article is solely governed by the terms of such publishing agreement and applicable law.

© The Author(s), under exclusive licence to Springer Nature America, Inc. 2025

Methods

Vascular fluorescent-gel-fill-based labeling

All experiments were performed on adult wild-type male mice (n = 23) aged between 50 and 80 days. Mice were housed on a 6:00 to 18:00 dark-light cycle, at an ambient temperature of 20.6–22.2 °C and humidity in the 30–65% range. All procedures adhered to the Guide for the Care and Use of Laboratory Animals and have been approved by the Institutional Animal Care and Use Committee at the University of California, San Diego.

Samples were prepared using a slightly modified version of our past procedures 8,36 . Mice were an esthetized with 2% (v/v) isoflurane in oxygen, administered an intraperitoneal injection of heparin (200 U) and overdosed with an intraperitoneal injection of Fatal-Plus. Exsanguination was carried out by transcranial perfusion. We used 60-150 ml oxygenated Ringers Carbicarb (37 °C) containing 10 U ml⁻¹ heparin peristaltically pumped at a rate of 18–21 ml min⁻¹ through a blunted 18-g cannula inserted through an incision made in the left ventricle; the right atria were snipped to provide an exit pathway for the exsanguinated blood. Exsanguination was judged complete by blood clearing of sternal vessels and of the dental pulp. Next, the head of the mouse was tilted down and 20 ml of fluorescently labeled gelatin (10% (w/v) porcine gelatin-0.4% (w/v) fluorescein isothiocyanate (FITC)-conjugated BSA in PBS-azide) was administered from a glass syringe-tubing assembly connected to the perfusion cannula in the left ventricle. At the end of perfusion, a small chip of dry ice was used to rapidly freeze the heart to minimize leakage of the warm gelatin through the perfusion incisions. The entire body was then placed upside down in an ice-filled bucket for 1 h to cool and solidify the intravascular gelatin. The head was removed and immersion-fixed by placing in cold paraformaldehyde/PBS for 48 h, followed by a cold PBS wash step for 48 h.

The gelatin solution was prepared by first blooming the porcine gelatin powder with cold PBS and then microwave-heating it to temperatures that did not exceed 60 °C. FITC-conjugated BSA in PBS-azide was added to liquefied gelatin that had been cooled to 37 °C. To minimize the occurrence of bubbles and occasional particulates in the resultant solution, the liquefied gelatin was sterile-filtered after rewarming in a 40 °C water bath. Residual air bubbles were then removed by suctioning the surface after centrifugation (3,000g, 2 min). The filtered labeled gelatin was held in a 40 °C water bath and transferred to a warmed glass syringe just before use.

Ablation system

The ablation module consisted of a Ti:sapphire ultrafast laser amplifier (Astrella, Coherent) running at 1 kHz with a pulse width of about 86 fs. The output beam of 11 mm in diameter $(1/e^2)$ was passed through a half waveplate mounted on a motorized rotational stage and split into two arms by a high-power polarizing beam splitter (PBS25-780-HP, Thorlabs). In the line-ablation configuration, a ×1.25 telescope was used for beam expansion and divergence adjustment. The S-polarized component was directed onto a reflective diffraction grating (830 mm, 53107ZD02-035R, Richardson Gratings) at 41.61° so that the principal diffracted beam propagated perpendicularly to the grating surface. The grating surface was conjugated to the objective image plane using a telescope in a 4f configuration with a long focal length lens. A 750-mm achromatic lens (AC508-750-B, Thorlabs) and a 700-mm cylindrical lens (LJ1836L1-B, Thorlabs) were used to form a plane and line-ablation pattern, respectively. Inserting or removing the diffuser (EDS-0.25, RPC Photonics) was automated using a motorized filter flip (MFF101, Thorlabs).

Flow system

Index-matching fluid in the reservoir was gravity-fed into a magnetic-driven pump (1/50 HP, 99845K46, McMaster-Carr) and pushed through an inline filter (5 μ m and 1 gal min $^{-1}$; 255575-75, Pentair/Pentek). Then, the flow was split into two channels with a custom flow

adapter manufactured using stereolithography (Accura ClearVue with Quick Clear finishing, Xometry). The narrower channel sent the fluid into the inline refractometer sensor before returning to the reservoir. The wider one passed through two check valves and an adjustable flowmeter, and reached a custom-designed objective nozzle. The objective nozzle channeled the flow through a narrow opening and formed a fan-shaped jet onto the objective front optical aperture. Liquid exited the nozzle through a wide opening in front of the aperture, forming a positive fluid pressure onto the sample. The sample was in a custom-designed holder, which drained the excessive liquid back to the reservoir. Both the objective cap and sample holder were manufactured using stereolithography (Accura ClearVue with Quick Clear finishing). A solid-state relay (G3NA-210B-UTU DC5-24, Omron) enabled the computer to control the pump.

Index-matching solution

We explored several index-matching solutions compatible with under-liquid femtosecond laser ablation. Sixty-seven per cent (v/v) TDE water solution is widely used for index matching, but its high viscosity prevents efficient removal of persistent bubbles; a 40% OptiPrep 60% (v/v) DMSO solution was used in serial two-photon imaging for its relatively high refractive index (RI) and compatibility with fluorescent proteins. However, we found a large number of persistent bubbles generated more than 100 µm below the focal plane with a modest ablation fluence (2 J cm⁻²). We selected 60% DMSO 40% (v/v) water with 10 mM HEPES buffer solution as our partial index-matching medium for its relatively high RI (n = 1.4286), low viscosity and compatibility with fluorescent proteins. For samples without fluorescent proteins, the concentration of DMSO could be increased to reach a higher RI and lower viscosity, although tissue deformation and water absorption might be an issue. For the 60% (v/v) DMSO solution, we found that 10 gal h⁻¹ of flow was necessary to reliably remove the persistent bubbles on the sample surface.

RI feedback control system

For multi-day continuous acquisition, maintaining the RI of the imaging immersion medium is crucial because RI drift alters objective magnification and introduces additional optical aberration. For an objective of a given NA, its focal length f shifts as the RI of the medium n changes according to the following relationship:

$$\frac{\delta f}{f} = \frac{n^2}{n^2 - NA^2} \frac{\delta n}{n}$$

In our case, $f = 7,200 \, \mu m$, n = 1.4286, NA = 1.0 and $\frac{\delta f}{f} \approx 2 \frac{\delta n}{n}$ or $\delta f \approx (10^4 \delta n) \, \mu m$. For the $60\% \, (\text{v/v})$ DMSO solution, we observed a 0.14% increase in RI over 24 h because water has a higher vapor pressure than DMSO.

We developed a custom unidirectional feedback control system to maintain the RI during the ablation process. The index-matching fluid pumped through the narrow channel was directed across the optical index measurement assembly of a digital handheld refractometer (MA871, Milwaukee Instruments) to measure its RI. To automate measurements, the refractometer's power and measurement buttons were replaced by N-channel metal-oxide-semiconductor field-effect transistors (MOSFETs) (IRL510, Vishay Siliconix) configured as voltage-controlled switches. We sent square wave pulses from the Vidrio DAQ board to the MOSFET gates, enabling software control of the refractometer. After the refractometer made a measurement, a USB camera took an image of the refractometer's LCD screen, which was processed in MATLAB to extract the measured Brix level and convert it to an RI. For precise camera alignment, we removed the LCD screen from the handheld refractometer and mounted it in a PLA 3D-printed housing that fixed its position relative to the camera. If the measured RI was greater than the desired set point, a solenoid valve (5001T42,

McMaster-Carr) controlled by the Vidrio DAQ board via a MOSFET was actuated to release water from a gravity-fed reservoir into the flow system.

Imaging system

The imaging system consisted of a four-channel two-photon microscope for high-resolution multiphoton imaging. The optical design was adapted from an in-house adaptive-optical two-photon microscope described earlier^{37,38}. The housing for detection optics was revised to accommodate 2-in optics and four symmetric detection channels. Sourced by an ultrafast laser oscillator (Chameleon Discovery NX, Coherent), the beam was expanded, reflected by a galvanometer scanner and an 8-kHz resonant scanner (Cambridge Technology), further expanded to fill the back aperture of the objective (XLSLPL-N25XGMP, NA = 1.0, 8-mm working distance, Olympus). A piezo stage (nPFocus400, NPoint) was used for fast Z-stack acquisition. Imaging signals were detected using Multi-Pixel Photon Counters (C13366-3050GA, Hamamatsu), amplified once using a voltage preamplifier (SR445A, Stanford Research System) and digitalized by a vDAQ (MBF Bioscience).

The imaging and ablation modules were combined just above the objective by switching between the primary dichroic (FF775-Di01-36×50, Semrock) and a mirror (PFR10-P01, Thorlabs) using a motorized actuator (NA11B60-T4A, Zaber). The sample was mounted on high-precision motorized linear stages with encoders (*xy*: LDA075A-AE53T10A; *z*: LRQ075AL-DE51CT10A; Controller: XMCC-4, Zaber).

Control software

We implemented the control software using object-oriented, event-triggered programming in MATLAB and off-loaded rate-limiting computation to Python processors for asynchronous parallel processing.

Single-layer imaging control

The microscope operates in two imaging modes: exploration and scanning. In both modes, the configuration space of the stage is discretized into a rectangular grid according to the acquisition parameters. Defining tile position using stage coordinates facilitates recovery from unanticipated operational disruptions and streamlines subsequent image stitching. The control pipeline maintains a queue of tiles (grid cells) for sequential acquisition, whose order is optimized to minimize distance and maximize unidirectional stage movement. In exploration mode, the microscope rapidly images the sample surface at low resolution to define the region of interest. Each acquired image tile is immediately analyzed based on voxel intensity statistics to determine whether the tile contains the sample. If so, its nearest neighboring tiles within the exploration space are added to the acquisition queue. The resulting exploration images are used to define the region of interest for the high-resolution scan.

The acquisition of each image tile was controlled by ScanImage (MBF Bioscience), which writes image data directly to a high-speed solid-state drive as TIFF files. During the acquisition of a single tile, the MATLAB process was not continuously occupied, although multiple timers periodically probed several systems states and detected hardware abnormalities. With up to four channels, the microscope could produce about 5 GB min⁻¹ of data. To overlap image processing with acquisition, with minimal performance impact on the control process in MATLAB, we implemented an asynchronous parallel processing pipeline in Python. This pipeline de-interleaved the TIFF stacks and saved the image to a network storage server in HDF5 format for its superior input/output performance. Concurrently, a downsampled version of the image stack, along with relevant descriptive statistics, was saved separately for computing the ablation mask. The processing status was relayed back to MATLAB via the transmission control protocol.

Single-layer ablation control

Heterogeneous biological tissues could have distinct optical and mechanical properties, such as soft brain parenchyma and rigid skull bone, even though they may be just micrometers apart. For precision ablation with minimal off-target damage, we fine-tuned ablation parameters such that the ablation fluences for each type of target were close to the damage threshold. High ablation precision comes with the requirements of detecting and ablating different targets at micrometer resolution in three dimensions. Consequently, the ablation process consists of 3D image analysis, motion planning, low-level hardware control sequence synthesis, execution and system state monitoring.

This process started with stitching the downsampled image tiles at 5-µm isotropic resolution using stage coordinates. A linear spectrum unmixing algorithm was applied to reduce crosstalk between detection channels. Subsequently, intensity-based channel-specific image segmentation algorithms determined the ablation volumes. The results were analyzed to identify ablation targets, including the skull, tissues in the skull cavities and brain tissues, which were summarized in a 3D labeled array.

Both the labeled array and the sets of ablation parameters specified the command sequence. For each ablation target, ablation parameters included fast axis speed, slow axis step size, z-step size and effective peak ablation fluence. The fast axis corresponds to the top linear stage, which can move fastest with the least load. At a given z-position, a two-dimensional mask of an ablation target at 1-µm resolution was computed from the labeled array via nearest neighbor interpolation. This two-dimensional mask was decomposed into parallel stripes along the fast axis. The widths of these stripes equaled the step size of the slow axis. For each stripe, the yintervals containing the ablation target were identified. The y position of the ablation target in the stripe defines the position of the triggering signal, while an additional acceleration/deceleration distance was added to both ends to ensure that the motorized stages reached a constant speed when the ablation laser was triggered. Lastly, we searched for an efficient route that traversed all intervals as a coverage path planning problem. Intervals were clustered into regions based on their spatial proximity and overlapping fractions. These regions formed the nodes in the traveling salesman problem, where the distance between two nodes is the minimal distance between any endpoints of these two regions. To specify the starting node and remove the requirement of returning to the starting point in the traveling salesman problem, a dummy node with zero distance from all the nodes, zero distance to the specific starting node and infinity distance to all the other nodes was introduced. The approximated shortest path traversing all regions was found using the 2-opt algorithm. For 3D ablation, the end position of the ablation path in the previous plane was used to initialize path planning in the current plane.

Finally, the path, triggering positions and kinematic parameters were sent to the stage controller stream buffer and executed. As the stage controller uses the idealized motion for trigger output, an additional offset was introduced to compensate for the delay between actual movement and the control input. This offset distance was empirically determined as the product of the typical delay time and the stage linear motion target speed.

Visual feedback for ablation quality control

When the ablation of a layer is complete, the microscope moves to the next layer (Extended Data Fig. 2a). As the ablation fluence is just slightly higher than the damage threshold while femtosecond laser ablation in an aqueous environment is a highly dynamic process, the variability in even a single type of biological tissue could give rise to local ablation failure. On the other hand, serial two-photon microscopy requires complete removal of the previous layer (n-1) before scanning the new layer (n). Otherwise, the residual tissue in layer (n-1) will reduce imaging quality and prevent precision ablation in the following layers; ablation in the subsequent layers will never be able to remove residues

(Extended Data Fig. 2b,c). To address this issue, we used the image acquired during the exploration mode in layer n for ablation quality control. If residual tissues were detected during exploration, the system reentered the ablation mode. During these refinement ablations, we also applied a depth-dependent ablation fluence, where targets further away from unimaged tissue are ablated with higher fluence (Extended Data Fig. 2f). Specifically, the ablation fluence at distance z from the last ablation plane F(z) is adjusted to

$$F(z) = F_0 e^{zk/l}$$

where F_0 is the normal ablation fluence of the targeted material, k is the number of ablation refinement iterations and $l = 200 \, \mu \text{m}$ is the exponential decay length. To eliminate the residual material from the prior layer, the ablation fluence on the first ablation plane was further amplified by 1.25^k . If large residuals far away from the boundary of the scan region of interest (Extended Data Fig. 2c,e) persist after three rounds of refinement ablation, the microscope moves back to the previous layer (red arrow in Extended Data Fig. 2a).

Hardware monitoring and imaging quality control

To guarantee long-term reliability, the status of the imaging laser was constantly monitored, with synchronous analysis of the acquired images for quality control. Communication between the controlling computer and the imaging laser was implemented using a serial port. A MATLAB timer was implemented to query and log laser states, including laser power, wavelength, shutter state and tuning state (Extended Data Fig. 2g). In scan mode, after acquiring each tile, we computed the maximum-intensity projection along the z-direction. This projection was analyzed to detect potential desynchronization between scanning and acquisition triggers. Detection of hardware malfunctions triggered a 're-image' notification to the controlling pipeline (red dots in Extended Data Fig. 2g).

Single-pulse ablation test

We characterized line-ablation using a fluorescent gelatin block in 60% (v/v) DMSO solution. After setting the focal plane to be about 10 μ m below the gelatin surface, we ablated six positions with a lateral step size of 20 μ m, using one pulse of fluence of 10 J cm⁻² at each. We imaged the volume before (I_0) and after (I_1) ablations at $0.25 \times 0.25 \times 1.0$ - μ m³ voxel resolution and measured the dimensions of the ablation site. We quantified the ablation volume by analyzing the intensity profile near the ablation site after taking the difference in the image stack ($I_1 - I_0$). The average projection along the y direction showed that all ablation sites were on the targeted ablation plane despite the uneven gelatin surface. Assuming a Gaussian intensity profile, we determined the FWHM of the ablation site along the x, y and z directions separately.

Continuous ablation test

The parameters for controlling the ablation process of one material are $(\gamma_t, \gamma_s, \Delta z, F)$ with the following definitions:

- y_f : numerical scalar representing the effective normalized ablation spot size along the fast axis. The translation speed of the stage $v_{abl} = \gamma_f d_f f_L$, where d_f is the effective diameter of the ablation volume along the fast axis and f_L is the repetition rate of the ablation laser and $d_f = D_f/\sqrt{2}$, where D_f is the $1/e^2$ diameter of the beam along the fast axis on the image plane. The factor of $\sqrt{2}$ results from the difference of a 'top hat' and Gaussian beam³⁹
- γ_s : numerical scalar, representing the effective normalized ablation spot size along the slow axis. The spacing between the ablation stripes $\Delta y = \gamma_s d_s$, where d_s is the effective diameter of the ablation volume along the slow axis, and $d_s = D_s/\sqrt{2}$, where D_s is the $1/e^2$ diameter of the beam along the slow axis on the image plane

- Δz: numerical scalar, representing the spacing between adjacent ablation sections
- F: numerical scalar, representing the estimated ablation fluence (1cm⁻²)

Gelatin blocks were machined with the (3.1, 0.75, 5 μ m, 10 J cm⁻²) parameters, and rodent skull was ablated with the (2.1, 0.5, 2 μ m, 2 J cm⁻²) parameters.

Planar ablation

We explored using a 600-mm grating (53107ZD02-351R, Richardson Gratings) and a 750-mm focal length achromatic spherical lens in the 4f system to produce a planar ablation pattern. However, this configuration produced a line-focusing pattern (0.1 × 8 mm²) on the back focal plane of the objective. Despite a significantly broadened pulse width on account of temporal focusing, we found laser-induced optical element damage inside the objective after continuous ablation. Testing several ablation powers, we observed that visible damage occurred after 15 min of ablation when the laser power at the back aperture was about 200 mW. We suspected that the damage resulted from optical glue absorbing light and accumulating heat, given that the damage correlated with both laser power and ablation duration, while the stretched pulse reduced the possibility of nonlinear absorption in transparent material. To avoid damaging the objective, we placed a small-angle (0.5° FWHM) diffuser close to the grating, which expanded the width of the line by about 60 times while preserving the ablation area on the image plane. Combined with a long working distance objective, this setup enabled continuous full power (~2,850 mW) ablation for hours without damaging the objective. Similarly, pairing a small-angle diffuser with a cylindrical lens in the 4f setup could transform the line-ablation pattern into a planar ablation pattern on the image plane.

We tested planar ablation on the gelatin block. Using spatiotemporally focused femtosecond pulses, we removed a volume of $700\times700\times50~\mu\text{m}^3$ of gelatin with the (0.71, 0.71, 10 μm , 7 J cm $^{-2}$) parameters, or effectively $3.2\times10^7~\mu\text{m}^3~\text{s}^{-1}$. This process produced a sharp lateral boundary between the ablated and intact regions. Despite the high lateral precision, the ablated surface showed fragmentation extending about 10 μm below the final ablation plane. While the bulk of material removal remained within 10 μm of the last ablated layer, some damage extended beyond 50 μm from this plane (Extended Data Fig. 5c,d).

Reporting summary

Further information on research design is available in the Nature Portfolio Reporting Summary linked to this article.

Data availability

The stitched data for the brain and skull in Fig. 3, at 1-µm isotropic resolution, is deposited on DANDI at https://doi.org/10.48324/dandi.001460/0.250703.1826 (ref. 40). The raw, unstitched data is 4 TB in size and is freely available upon request from the authors.

Code availability

The code is available at https://github.com/xiangjiph/WBIM_public and as Supplementary Code 1. The software is distributed under the terms of the BSD 3-Clause License.

References

- Blinder, P. et al. The murine cortical angiome: an interconnected vascular network with noncolumnar patterns of blood flow. *Nat. Neurosci.* 16, 889–897 (2013).
- Liu, R., Li, Z., Marvin, J. S. & Kleinfeld, D. Direct wavefront sensing enables functional imaging of infragranular axons and spines. *Nat. Methods* 16, 615–618 (2019).

- Yao, P., Liu, R., Broginni, T., Thunemann, M. & Kleinfeld, D. Construction and use of an adaptive optics two-photon microscope with direct wavefront sensing. *Nat. Protoc.* 18, 3732–3766 (2023).
- ISO 21254-1:2025. Lasers and laser-related equipment test methods for laser-induced damage threshold. Part 1: definitions and general principles. *International Organization for Standardization* www.iso.org/standard/83937.html (2025).
- Ji, X., Huang, S., Friedman, B. & Kleinfeld, D. Craniocerebral skull and vasculature stitched datasets. *DANDI* https://doi. org/10.48324/dandi.001460/0.250703.1826 (2025).

Acknowledgements

We thank R. Liu for advice on optical design, C. Xu for technical discussions and R. Figueroa-Mercado and M. Moreno for assisting with the sample preparations. This study was funded by a National Institutes of Health BRAIN Initiative grant no. U19 NS123717, a National Institute of Neurological Disorders and Stroke grant no. R35 NS097265 to D.K. and a Predoctoral Fellowship (no. 906077) from the American Heart Association to X.J. The funders had no role in study design, data collection and analysis, decision to publish or preparation of the manuscript.

Author contributions

D.K. conceived the project. X.J. and S.H. designed the hardware. X.J. designed the software. B.F. produced the samples. X.J. and S.H. conducted the experiments and analyzed the data. X.J. and D.K.

wrote the paper with input from B.F. and S.H. D.K. further attended to the university rules and forms that govern environmental health and safety, including the ethical use of animals, the use of chemicals, controlled substances, hazardous substances, lasers and viruses, and the maintenance of cybersecurity.

Competing interests

The authors declare no competing interests.

Additional information

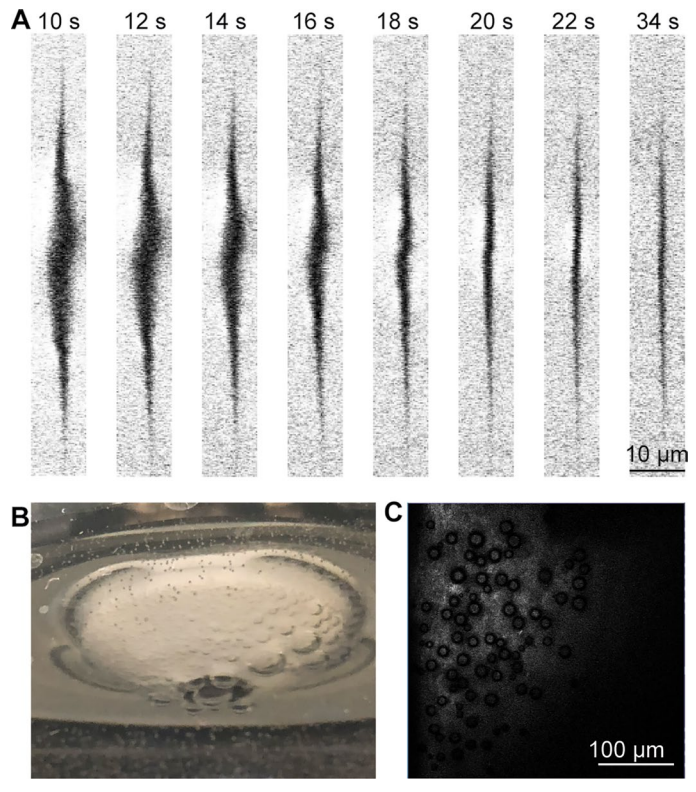
Extended data is available for this paper at https://doi.org/10.1038/s41592-025-02849-2.

Supplementary information The online version contains supplementary material available at https://doi.org/10.1038/s41592-025-02849-2.

Correspondence and requests for materials should be addressed to Xiang Ji or David Kleinfeld.

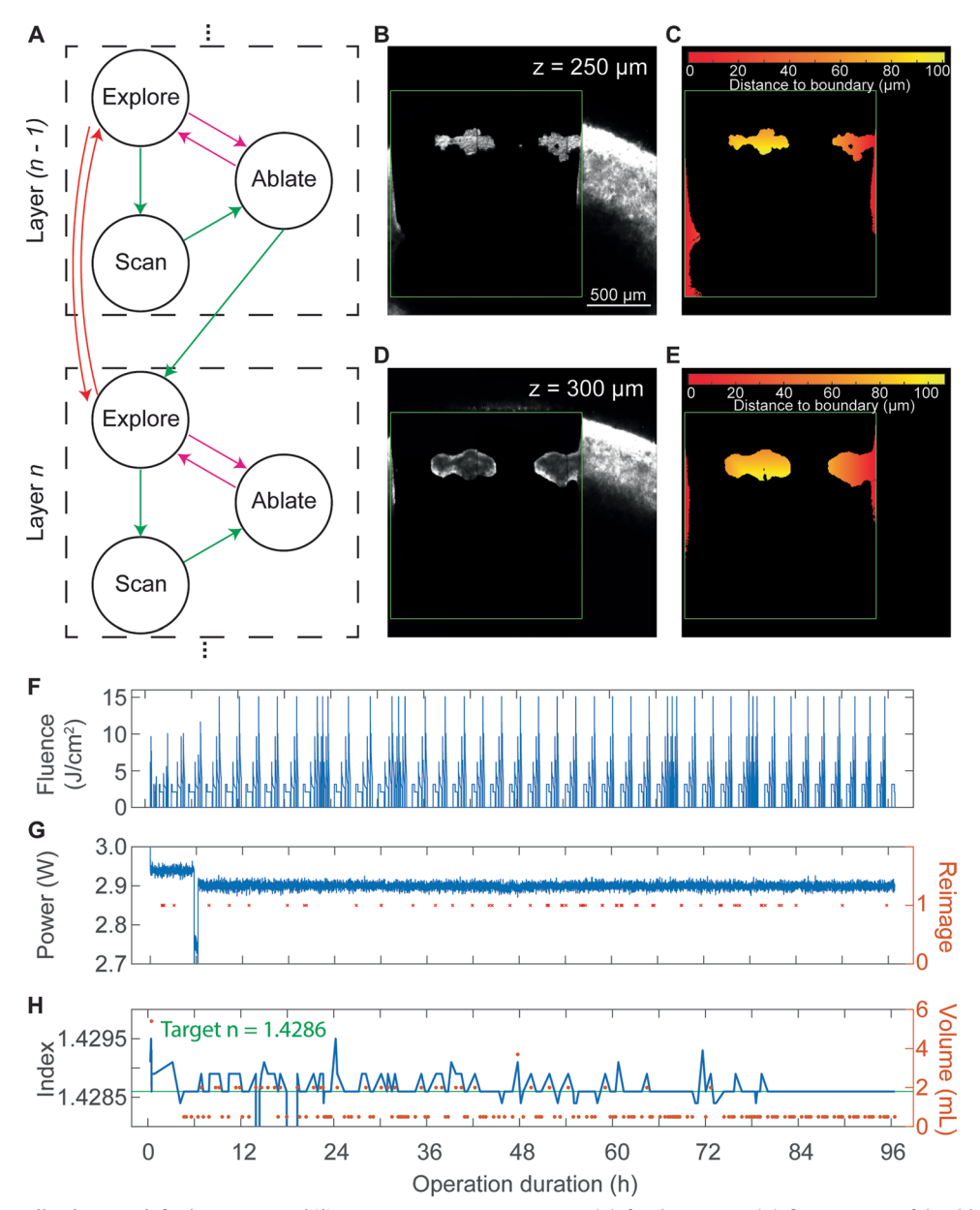
Peer review information *Nature Methods* thanks Adam Glaser and the other, anonymous, reviewer(s) for their contribution to the peer review of this work. Peer reviewer reports are available. Primary Handling Editor: Nina Vogt, in collaboration with the *Nature Methods* team.

Reprints and permissions information is available at www.nature.com/reprints.



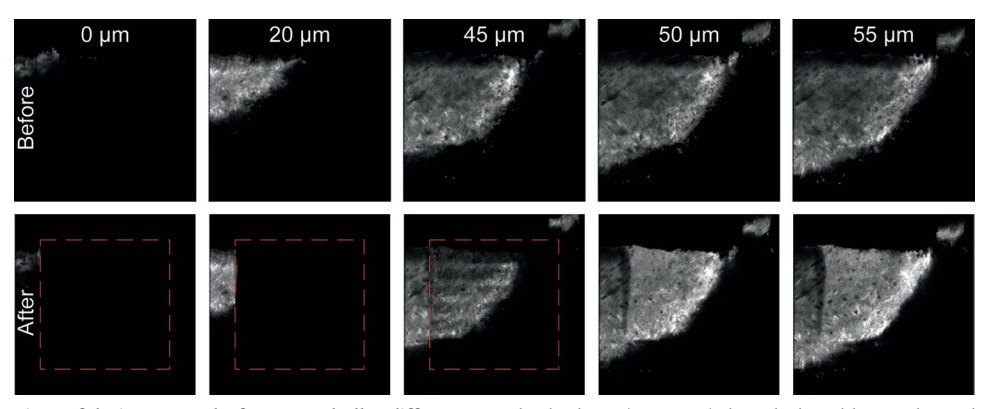
 $\label{lem:extended} \textbf{Extended Data Fig. 1} | \textbf{Femtosecond pulses generate bubbles in the immersion media. a}. \\ \textbf{Image of an ablation site on gelatin block surface at different time points after single pulse ablation (2 J/cm²). \\ \textbf{The darkness is caused by slowly dissolving bubbles}. \\ \textbf{The length of the line was limited by truncating the beam}$

width to 2.54 mm before the grating. The pump was off during this experiment. **b.** Bubble accumulation on the front optical aperture. **c.** Bubble accumulation on skull surface without flow.



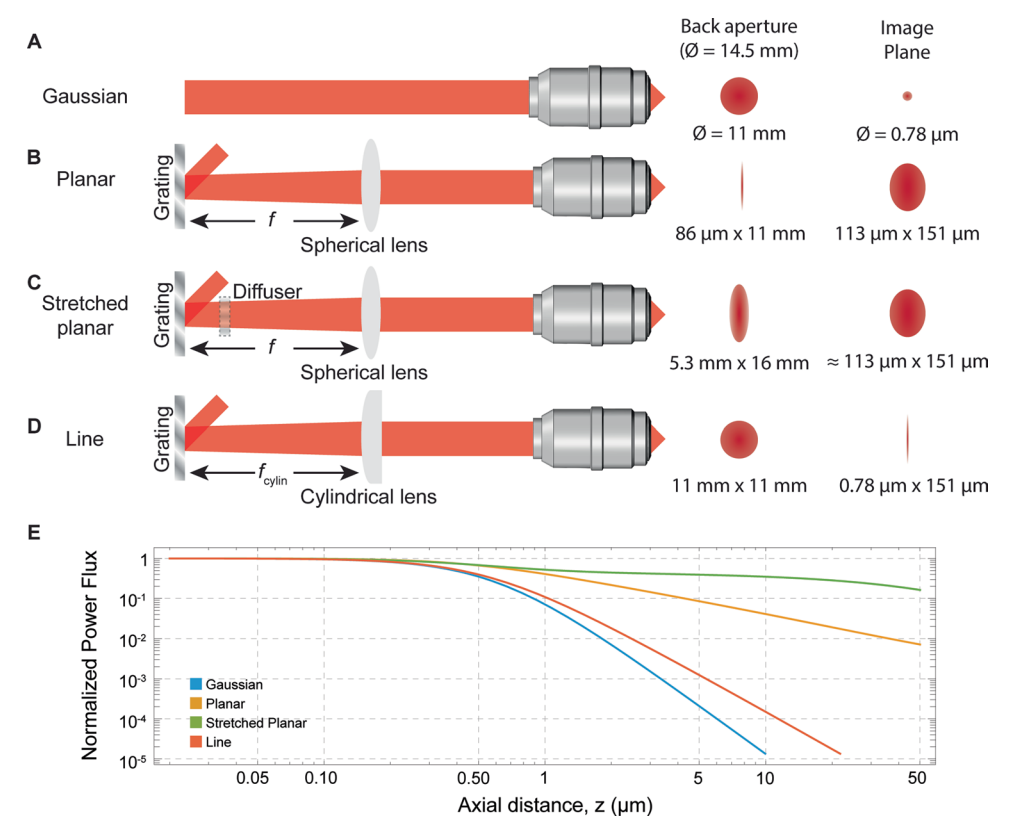
Extended Data Fig. 2 | Feedback controls for long-term stability. a. System state work flow. Acquisition is divided into multiple layers. Normal work flow (green arrows) involves iterative exploration, scanning, and ablation. Exploration results are also used for machining quality control (red arrows). b. Single section of exploration image stacks after ablation. ROI for high-resolution scanning is green boxed. In this ROI, there exists residual skull components which were not successfully removed in the previous round of ablation. c. The software analyzes the distance between the residuals and the boundary of the scan ROI. Based on this analysis, the control pipeline determines the next operation. d. Same as (B) but at 50 μ m below (B). Residual components typically grow larger with depth.

 $e. Same \ as \ (C), for the image in (D). \textbf{f}. Time series of the ablation fluence used over the course of a 96-hour-long operation. Fluence is adjusted based on ablation target and the ablation results in the previous ablations. \textbf{g}. Time series of the imaging laser power (left y axis) and the imaging state (right y axis) over the course of a 96-hour-long operation. The microscope re-images the tile when power becomes unstable, or the imaging triggering signals become desynchronized. \textbf{h}. Time series of the immersion refractive index (RI, left y axis) over the course of a 96-hour-long operation (mean 1.4287; SD 0.00022). RI was measured when the pump was turned on and RI is adjusted by adding H2O (right y axis) when the measured RI deviates from the target RI (1.4286).$



Extended Data Fig. 3 | Sections of the image stack of a mouse skull at different depths before versus after continuous ablation. In the first column (z = 0 μ m) the red dotted box indicates the first ablation plane. The red dotted box in the

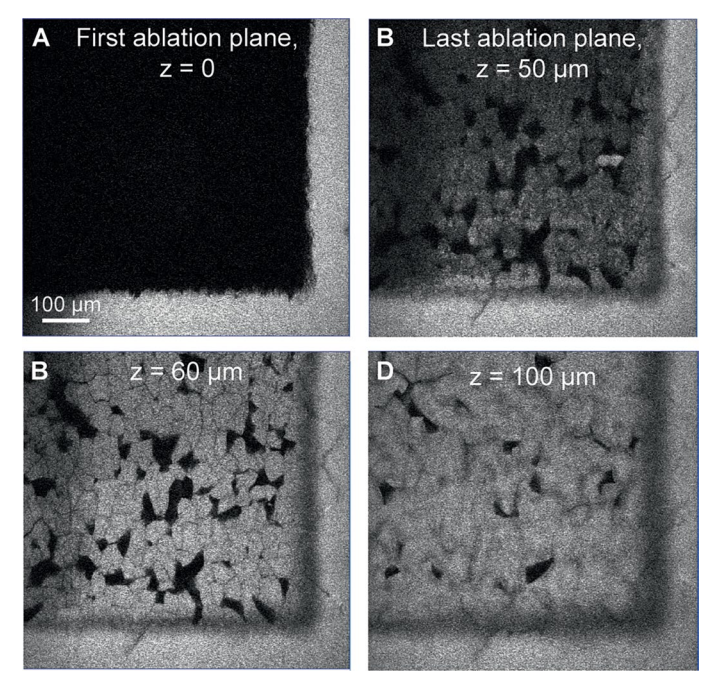
third column (z = 45 μ m) show the last ablation plane. The 4th column shows intact skull structure 5 μ m below the last ablation plane. Ablation parameters: (2.1, 0.5, 2 μ m, 2 J/cm²) with a line ablation pattern; see Supplementary Table 2.



Extended Data Fig. 4 | Comparing femtosecond laser ablation configurations.

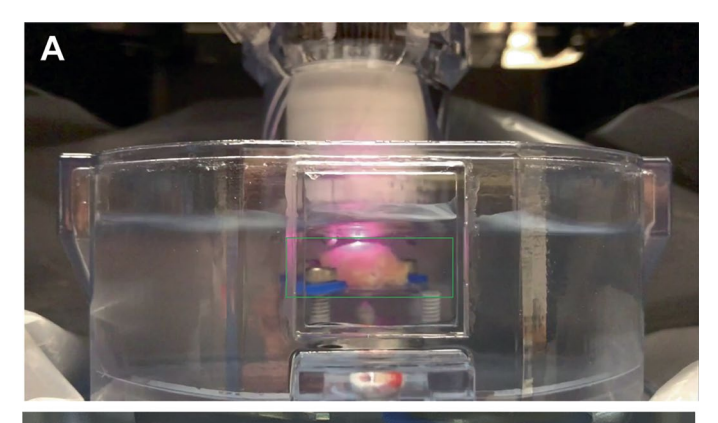
a. A Gaussian beam produces sub-micrometer-sized ablation spot on the image plane. All estimations in this figure are based on a beam with an 11 mm diameter, a 7.2 mm focal length, 1.0 NA objective, a reflective grating with groove density 830/mm, a spherical or cylindrical lens with a 700 mm focal length. All beam dimensions refer to $1/e^2$ diameters, which are $\sqrt{2}$ larger than the effective diameter used to characterize the ablation volume. Actual experimental parameters may vary. **b.** A spherical lens focuses the diffracted beam into a line

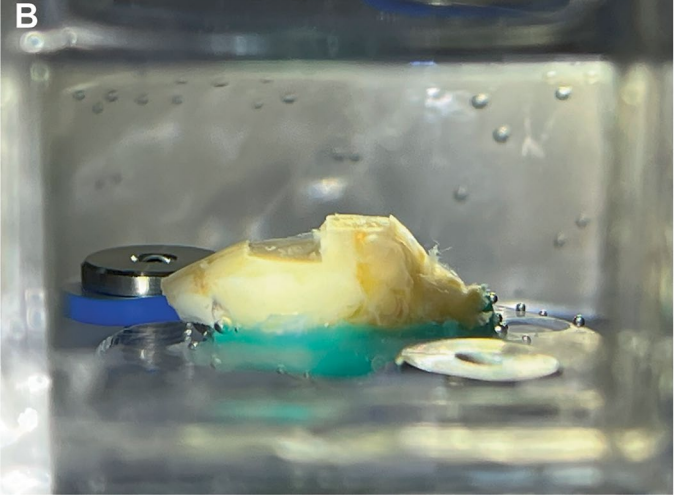
on the back focal plane of the objective and an elliptical planar pattern on the image plane. **c**. Adding a small angle diffuser (FWHM 0.25 degrees) near the diffractive grating produces an elliptical pattern on both the back and front focal plane of the objective, preventing accumulated heat from damaging objective. **d**. Combining a cylindrical lens and the objective produces a line ablation pattern. **e**. Comparison of the axial confinement of the normalized power flux of each configuration.



 $\label{lem:extended} \textbf{Data Fig. 5} | \textbf{Continuous gelatin ablation using a planar ablation} \\ \textbf{pattern. a}. \\ \textbf{Image of the sample on the first ablation plane, showing clear ablation} \\ \textbf{volume boundary. b. } \\ \textbf{Image of the sample on the last ablation plane, which is} \\ \textbf{absolute the plane of the sample on the last ablation plane, which is} \\ \textbf{b. } \\$

 $50~\mu m$ below the first ablation plane in (A). c. Image of the sample on a plane $10~\mu m$ below the last ablation plane. d. Image of the sample on a plane $50~\mu m$ below the last ablation plane, showing significant out-of-focus ablation damage.





Extended Data Fig. 6 | In situ all optical histology. a. Femtose cond laser machining of mouse skull and brain (green box). Laser (purple light) is triggered when the targeted region of the sample crosses the focal area of the objective. b. A mouse brain within the skull after multiple iterations of imaging and ablation.

nature portfolio

Corresponding author(s):	David Kleinfeld Xiang Ji
Last updated by author(s):	05/22/2025

Reporting Summary

Nature Portfolio wishes to improve the reproducibility of the work that we publish. This form provides structure for consistency and transparency in reporting. For further information on Nature Portfolio policies, see our <u>Editorial Policies</u> and the <u>Editorial Policy Checklist</u>.

_					
C -	1	т	C	ь.	CS
	М				1 >

For	For all statistical analyses, confirm that the following items are present in the figure legend, table legend, main text, or Methods section.				
n/a	Confirmed				
	The exact	sample size (n) for each experimental group/condition, given as a discrete number and unit of measurement			
	🔀 A stateme	nt on whether measurements were taken from distinct samples or whether the same sample was measured repeatedly			
		ical test(s) used AND whether they are one- or two-sided on tests should be described solely by name; describe more complex techniques in the Methods section.			
\boxtimes	A description of all covariates tested				
\boxtimes	A description of any assumptions or corrections, such as tests of normality and adjustment for multiple comparisons				
\boxtimes	A full description of the statistical parameters including central tendency (e.g. means) or other basic estimates (e.g. regression coefficient) AND variation (e.g. standard deviation) or associated estimates of uncertainty (e.g. confidence intervals)				
\boxtimes	For null hypothesis testing, the test statistic (e.g. <i>F</i> , <i>t</i> , <i>r</i>) with confidence intervals, effect sizes, degrees of freedom and <i>P</i> value noted Give <i>P</i> values as exact values whenever suitable.				
\boxtimes	For Bayesian analysis, information on the choice of priors and Markov chain Monte Carlo settings				
\boxtimes	For hierarchical and complex designs, identification of the appropriate level for tests and full reporting of outcomes				
\boxtimes	\square Estimates of effect sizes (e.g. Cohen's d , Pearson's r), indicating how they were calculated				
	•	Our web collection on <u>statistics for biologists</u> contains articles on many of the points above.			
Software and code					
Policy information about <u>availability of computer code</u>					
Da	Data collection https://github.com/xiangjiph/WBIM_public; ScanImage 2022.1.0;				
Da	ata analysis	https://github.com/xiangjiph/WBIM_public			

For manuscripts utilizing custom algorithms or software that are central to the research but not yet described in published literature, software must be made available to editors and reviewers. We strongly encourage code deposition in a community repository (e.g. GitHub). See the Nature Portfolio guidelines for submitting code & software for further information.

Data

Policy information about <u>availability of data</u>

All manuscripts must include a data availability statement. This statement should provide the following information, where applicable:

- Accession codes, unique identifiers, or web links for publicly available datasets
- A description of any restrictions on data availability
- For clinical datasets or third party data, please ensure that the statement adheres to our policy

The stitched data for the brain and skull in Fig. 3, at 1-μm isotropic resolution, is deposited on DANDI at https://doi.org/10.48324/dandi.001460/0.250703.1826.

Human rese	earch part	icipants
Policy information	about <u>studies</u>	involving human research participants and Sex and Gender in Research.
Reporting on sex and gender		N/A
Population characteristics		N/A
Recruitment		N/A
Ethics oversight		N/A
Note that full informa	ation on the app	proval of the study protocol must also be provided in the manuscript.
	. •	
Field-spe	ecific re	eporting
	ne below that	is the best fit for your research. If you are not sure, read the appropriate sections before making your selection.
Life sciences		Behavioural & social sciences
For a reference copy of	the document wit	h all sections, see <u>nature.com/documents/nr-reporting-summary-flat.pdf</u>
Lifo scior	acoc ct	udy design
	N/A	e points even when the disclosure is negative.
Sample size		
Data exclusions	N/A	
Replication	N/A	
Randomization	N/A	
Blinding	N/A	
Reportin	g for s	pecific materials, systems and methods
		s about some types of materials, experimental systems and methods used in many studies. Here, indicate whether each material,
system or method list	ted is relevant t	o your study. If you are not sure if a list item applies to your research, read the appropriate section before selecting a response.
Materials & ex	perimental	systems Methods
n/a Involved in the study		n/a Involved in the study
Antibodies		ChIP-seq
Eukaryotic cell lines		Flow cytometry
Palaeontology and archaeology MRI-based neuroimaging Animals and other organisms		
	_	ms .
Clinical dat	ta esearch of conc	orn.
NA Dagi ase is	escuren or conc	
Animals and	l other re	search organisms
Policy information Research	about <u>studies</u>	involving animals; ARRIVE guidelines recommended for reporting animal research, and Sex and Gender in
Laboratory anima		experiments were performed on adult wild-type male mice aged between 50-80 days. The housing conditions for the mice led a 6 AM to 6 PM dark/light cycle, ambient temperature of 690 to 720 F, and humidity in the range of 30 % to 65 %.

Wild animals

N/A

Reporting on sex	N/A
Field-collected samples	N/A
Ethics oversight	The Institutional Animal Care and Use Committee at the University of California, San Diego (UCSD)

Note that full information on the approval of the study protocol must also be provided in the manuscript.